A New Constitutive Model for the Finite Element Simulation of Local Hot Forming of Aluminum 6xxx Alloys

S. GOUTTEBROZE, A. MO, Ø. GRONG, K.O. PEDERSEN, and H.G. FJÆR

A new internal variable constitutive model for the use in finite element (FE) simulation of local hot forming of 6xxx aluminum alloys is presented. The model relates the flow stress to the temperature, total strain rate, and internal variables, which represent the dislocation density and the contributions to the hardening stress from elements in solid solution and precipitates. The time evolutions of the internal variables are modeled by an equation representing the accumulation/annihilation of dislocations and by a precipitate model developed elsewhere, taking into account a size distribution of precipitates. The parameters of the constitutive model have been fitted to tensile tests at different temperatures, strain rates, and precipitate states.

DOI: 10.1007/s11661-007-9443-8

I. INTRODUCTION

DURING recent years the automotive industry, as well as the component and product suppliers, have greatly increased their use of aluminum. New designs and applications require new forming operations. Among these we find the local hot forming process in which the material is subjected to local heating while being simultaneously deformed, either thermally induced or by an additional mechanical load. By hot forming, the softening behavior that some alloys exhibit at elevated temperatures is exploited in order to effectively carry out certain critical forming operations (*e.g.*, deep drawing[1] or hydroforming[2]) or controlling the local microstructure,[3] and thus the local properties of the final component. Moreover, the use of local hot forming also allows drawing without die or backing tool, which is a great advantage when extruded sections are deformed.[4]

The advanced use of mathematical models and associated finite element (FE) codes can be a great help when the benefits of local hot forming are to be exploited. Critical parts of such models, though, are the constitutive equations by which the flow stress associated with the viscoplastic deformation is related to the viscoplastic strain rate, temperature, and microstructure.

The challenge associated with establishing accurate and reliable constitutive equations for modeling hot forming of age-hardened aluminum alloys is that the flow stress changes not only due to the creation and annihilation of dislocations (*i.e.*, strain hardening and recovery[5,6]), but also due to changes in the volume fraction and size distribution of the hardening precipitates.[7] Both factors have a significant influence on the value of the local flow stress due to complex interactions between the precipitates and the dislocations.[8]

The purpose of this article is to present a new constitutive model for the application in simulations of hot forming of aluminum 6xxx alloys. By means of internal variables, this model accounts at the continuum level for the previously mentioned effects that the evolving microstructure may have upon the viscoplastic flow stress. The new model is based upon existing models accounting for strain hardening and recovery[6,8] and the precipitation of particles from solute elements[7,9–11] and their contribution to the yield stress.[12,13] Furthermore, the present model intends to calculate the instantaneous flow stress for typical values of the temperatures and strain rates and their variation with time in a similar manner as in local hot forming operations. This is different from most existing models, which are mainly defined by constitutive equations that can adequately fit the stress-strain curves obtained in mechanical tests carried out at various, but constant, temperatures and strain rates.

To the knowledge of the authors, no existing constitutive model can be directly implemented in a FE code in order to satisfactorily take into account the previously mentioned microstructural aspects and their influence on the flow stress in simulations of hot forming operations. The most recent simulation work directed toward deep drawing, for example, is limited in temperature and do not simulate precipitate evolution.[14] In a previous article on modeling the microstructure and strength evolution in age-hardened aluminum alloys,[11] the development of precipitates was taken into account in FE simulations of multistage thermal processing (artificial age-hardening, welding, and postwelding heat treatment), however, only a relatively simple empirical model was used to account for the dislocation hardening.

S. GOUTTEBROZE, Research Scientist, is with SINTEF, P.O. Box 124, Blindern, N-0314, Oslo, Norway. A. MO, Research Manager and Adjunct Professor, is with SINTEF and the University of Oslo, P.O. Box 124, Blindern, N-0314, Oslo, Norway. Ø. GRONG, Professor, is with the Department of Materials Science and Engineering, NTNU, Alfred Getz vei 2, N-07491, Trondheim, Norway. K.O. PEDERSEN, Senior Scientist, is with SINTEF, Alfred Getz vei 2, N-07491, Trondheim, Norway. H.G. FJÆR, Senior Scientist, is with the Institute for Energy Technology, Postboks 40, N-2027, Kjeller, Norway.

Manuscipt submitted March 22, 2007.
Article published online January 26, 2008

The new constitutive model is presented in Section II, and Section III is devoted to fitting the model to an existing set of experimental data.[15] Although the applied data set is limited to relatively small strain rates (from 10^{-4} s^{-1} to 10^{-2} s^{-1}) and temperatures below 340 °C, we believe that the model could give valuable results also at higher temperatures and strain rates. This is because the model becomes equivalent to the well-established Zener–Hollomon relation[16] in the limit of stationary creep taking place at high temperatures. This relation is valid for a wide range of temperatures and strain rates. The new constitutive model and its main hypotheses are discussed in Section IV. A modeling example is then carried out in Section V in which the developments of microstructure and flow stress are calculated by the new model, using as an input history of temperature and strain rate that is relevant for local hot forming processes. A conclusion along with some suggestions for further research is presented at the end.

II. THE NEW CONSTITUTIVE MODEL*

*Please note that all mathematical symbols are defined both in the text and in Table I. This table summarizes all variables and parameters, including references to where the parameter values have been taken from.

A. *Kinetic Equation*

The viscoplastic equivalent strain rate $\dot{\varepsilon}^p$ and equivalent flow stress σ are related to each other by a kinetic equation in which both forest dislocations and precipitates contribute to the hardening. As a starting point, we have adopted the kinetic equation originally proposed by Estrin:[6]

$$\sigma = \hat{\sigma}\left(\frac{\dot{\varepsilon}^p}{\dot{\varepsilon}_0}\right)^{1/m} \qquad [1]$$

where $\hat{\sigma}$ is the hardening stress representing the material state, and $\dot{\varepsilon}_0$ and m are material parameters. The parameter m is strongly dependent on temperature, while $\dot{\varepsilon}_0$ is assumed constant. Internal variables characterize the material state; they represent the forest dislocation density ρ, and the contribution to $\hat{\sigma}$ from the elements in solid solution σ_s, and the precipitates σ_p.[5,6] The precipitate model is described in more detail in Section II–C.

The different hardening contributions are added (the intrinsic strength of the lattice is neglected) to yield

$$\hat{\sigma} = \sigma_\perp + \sigma_s + \sigma_p = M\alpha G\mathbf{b}\sqrt{\rho} + \sigma_s + \sigma_p \qquad [2]$$

where the first term represents the interaction between dislocations. Furthermore, **b**, M, G, and α are burger's vector, the average Taylor factor, the shear modulus, and a numerical constant, respectively. All of these material parameters are assumed constant.

Please note that some authors[8,17] put σ (instead of $\hat{\sigma}$) on the left-hand side of Eq. [2] without introducing the kinetic equation (Eq. [1]) at all. This is an acceptable approximation only at low temperatures for which the strain rate dependency of the flow stress is small, *i.e.*, $\left(\frac{\dot{\varepsilon}^p}{\dot{\varepsilon}_0}\right)^{1/m} \approx 1,\ \forall\dot{\varepsilon}^p$, as illustrated in Figure 1.

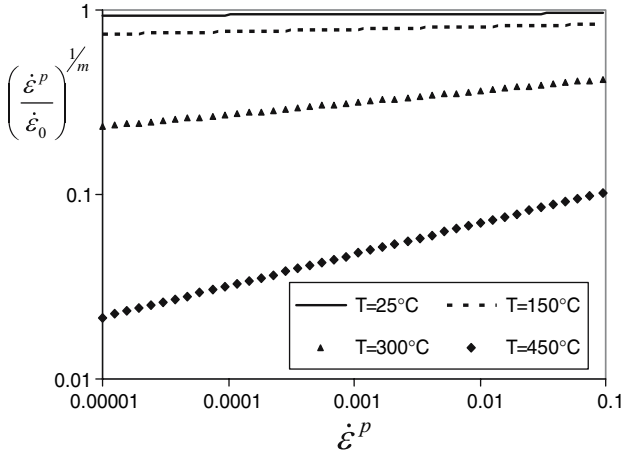

Fig. 1—Evolution of the strain rate sensitivity term at different temperatures.

While Eqs. [1] and [2] can easily give a reasonably good fit to experimental data at lower temperatures,[6,8] they tend to overestimate the dislocation density and thereby $\sigma_\perp$ and $\hat{\sigma}$ at higher temperatures. To illustrate this problem, we start by noting that the factor $\left(\frac{\dot{\varepsilon}^p}{\dot{\varepsilon}_0}\right)^{1/m}$ in Eq. [1] mainly represents the strain rate sensitivity. The parameter m can thus be estimated from tensile testing with a jump in strain rate at different temperatures, assuming that the hardening stress, *i.e.*, the other factor in Eq. [1] ($\hat{\sigma}$) remains approximately constant during the transient time associated with the increase in strain rate from the first constant value to the other. The factor $\hat{\sigma}$ can then be calculated by Eq. [1] as illustrated in Figure 2. In the lower temperature case in this figure, obtained by using a test specimen in the T6 temper (experiment B-ini, Table II in Section III–A), the high $\hat{\sigma}$ value is easily explained by the strong precipitate hardening and by a relatively high dislocation density. At the higher temperature, on the other hand (experiment D-SSS, Table II in Section III–A), the hardening precipitates have been dissolved, leading to $\sigma_p \approx 0$, while the estimated $\hat{\sigma}$ still has a relatively high value. Equation [2] then predicts a dislocation density during deformation at the higher temperature that is even higher than at the lower temperature. This is in contradiction to the expected low value and increase in dislocation density associated with straining at the higher temperature.

To solve this problem, we have multiplied the right-hand side of Eq. [1] with a temperature dependent factor χ. The new kinetic equation then becomes

$$\sigma = \chi(T)\hat{\sigma}\left(\frac{\dot{\varepsilon}^p}{\dot{\varepsilon}_0}\right)^{1/m} \qquad [3]$$

where $\hat{\sigma}$ becomes the hardening stress at room temperature. The slight temperature dependency of the shear modulus is also included in χ. At low temperature, this new formulation must become equivalent to the classical

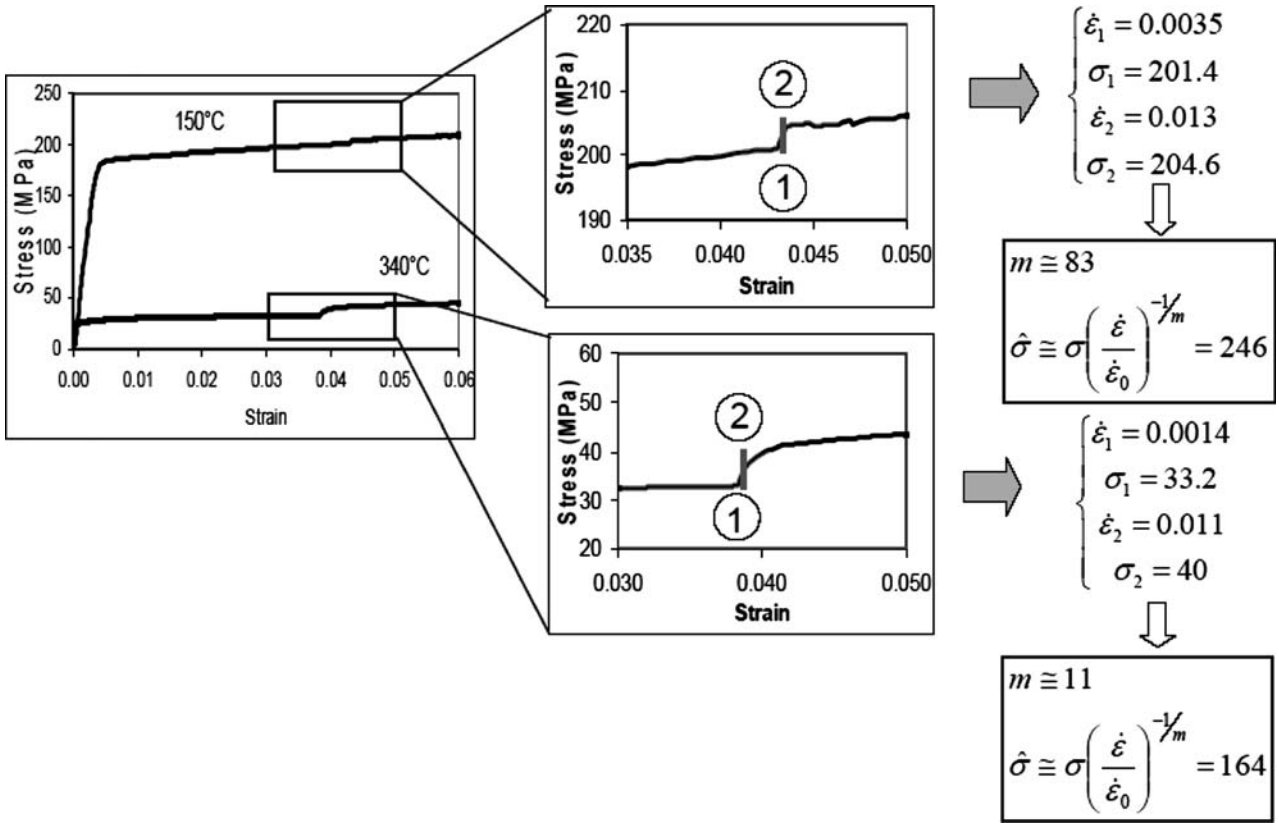

Fig. 2—Estimate of the strain rate sensitivity and hardening stress at different temperatures. Experimental data are taken from Ref. 15.

formulation, and thus χ tends toward 1 when the temperature decreases. Further details on $\chi(T)$ will be discussed in Section III.

B. *Dislocation Hardening and Recovery*

The dislocation hardening and the recovery are modeled by a change in the dislocation density exactly as proposed by Estrin.[6] The evolution equation of the dislocation density is†

$$\frac{\partial \rho}{\partial t} = \left[k_1 \sqrt{\rho} - k_2 \rho \right] \dot{\varepsilon}^p \qquad [4]$$

where the two terms represent a competition between storage of mobile dislocations and dynamic annihilation of dislocations. The first term is proportional to the mean free path of mobile dislocations, which in turn is proportional to the square root of the dislocation density, and the second term is proportional to the dislocation density. While the coefficient k_1 is taken to be constant, k_2 depends on both temperature and viscoplastic strain rate.[6]

In this model, only the "dynamic part" of the recovery is taken into account. Here we define dynamic recovery as a microstructural change that occurs only if the viscoplastic strain rate $\dot{\varepsilon}^p$ is nonzero. It dependents on viscoplastic strain rate and temperature. In the literature,[6] however, an additional term is often introduced to model the so-called "static recovery," which is a thermally-activated recovery process. This term, which is nonzero even when $\dot{\varepsilon}^p = 0$, represents the only active mechanism that leads to a decrease in the dislocation density during heat treatment of a stress-free material. Static recovery is neglected here, which means that the model may overpredict the dislocation hardening in, *e.g.*, the case of straining at low temperature followed by heating.

A straightforward way to determine k_1 and k_2 for a given alloy would be to model given experimental tests (*e.g.*, tensile tests at different constant values of temperature and strain rate being within the interval of interest for the use of the model), and then tune the coefficients of the constitutive model for optimal correspondence between modeling and experimental results. However, because k_2 depends on both temperature and viscoplastic strain rate, such a procedure would be relatively complicated, and various relations between k_2 and these two quantities would be possible. To simplify and guide the fitting procedure, we have therefore imposed the well-known Zener–Hollomon[16] or Garofalo's equation[18] to apply in the saturation stress limit, *i.e.*, when $\frac{\partial \rho}{\partial t} \rightarrow 0$ where the dislocations are recovered at the same

†Please note that Estrin[6] writes the evolution equation on a form obtained by subdividing Eq. [4] by $\dot{\varepsilon}^p$, while the present authors prefer a "rate form" more in line with most other internal variable formulations.

rate as they are created. Equation [4] with a zero left side leads to

$$k_2 = \frac{k_1}{\sqrt{\rho^*}} \quad [5]$$

where the saturation value $\sqrt{\rho^*}$ is given by the combination of Eqs. [2] and [3]:

$$\sqrt{\rho^*} = \frac{\sigma^* \chi [T]^{-1} \left(\frac{\dot{\varepsilon}^p}{\dot{\varepsilon}_0}\right)^{-1/m} - \sigma_s^{ss}}{M \alpha G \mathbf{b}} \quad [6]$$

with

$$\sigma^* = a \cdot \mathrm{asinh}\left[(ZH)^{1/n}\right] \quad [7]$$

While Zener–Hollomon is further defined and discussed subsequently, the factor σ_s^{ss} refers to the value of σ_s where all the precipitates are dissolved ($\sigma_p = 0$). This material state corresponds to high temperatures at which experiments for determining the parameters in the Zener–Hollomon relation are normally carried out. Moreover, the Zener–Hollomon relation *per se* represents useful input to the saturation stress at high temperatures and strain rates, which complete the limited experimental data available in most parameter fitting processes, including the one presented in Section III of the present article.

The dislocation density at saturation σ^* is assumed independent of the precipitate state as its value is based on the solid solute state. Nevertheless, the corresponding saturation stress σ^* is dependent on the precipitate state because the hardening stress in Eq. [2] is the summation of the dislocation stress $\sigma_\perp$, the *current* solid solution stress σ_s, and precipitate stress σ_p, which is nonzero as soon as precipitation occurs.

According to Miller,[19] the temperature dependence of steady-state deformation does not exactly follow an exponential law at the lower temperatures. A similar observation was made in the present study, and Zener–Hollomon in Eq. [7] is thus approximated by an equation similar to, but slightly different from, that in Reference 19, and that is more easily fitted to our experimental data

$$\mathrm{ZH} = \frac{\dot{\varepsilon}^p}{A} \, m\mathrm{in}\left[\exp\left(\frac{Q}{\mathrm{R}T}\right), \exp\left(\frac{Q}{RT_c}\,\frac{T_c + 770[\mathrm{K}]}{T + 770[\mathrm{K}]}\right)\right] \quad [8]$$

where T_c is a critical temperature fixed at 150 °C (423 K in Eq. [8]).

C. *Precipitation Model*

The precipitation model describes the nucleation, growth, and coarsening of precipitates. The model is taken from References 10 and 11 and only briefly summarized here. The process is controlled by the solute concentration and consequently by the temperature. The particles are assumed spherical and with uniform thermodynamic properties. New stable particles with radius r^* nucleate at a rate j given by

$$j = j_0 \exp\left[-\left(\frac{A_0}{\mathrm{R}T}\right)^3 \left(\frac{1}{\mathrm{In}\left(\overline{C}/C_e\right)}\right)^2\right] \exp\left(-\frac{Q_d}{RT}\right) \quad [9]$$

where Q_d is the activation energy for diffusion, and A_0 and j_0 are numerical parameters. The quantities $\overline{C}$ and C_e are the mean concentration and the equilibrium concentration at the interface, respectively, and $\overline{C}$ is calculated by

$$\overline{C} = C_0 - \left(C_p - \overline{C}\right) \int_0^\infty \frac{4}{3} \pi r^3 \varphi dr \quad [10]$$

where C_i and C_p are the concentration at the interface and inside the particle, respectively, and φ is the size distribution function.

Both j and r^* are temperature and concentration dependent. At each temperature, r^* is deduced from a particle growth model stating that the particles will dissolve or grow depending on the matrix and interface concentrations according to

$$\frac{dr}{dt} = \frac{\overline{C} - C_i}{C_p - C_i} \, \frac{D}{r} \quad [11]$$

where D is the diffusion coefficient. The parameter r^* corresponds to $\frac{dr}{dt} = 0$ and thus $\overline{C} = C_i$, where C_i is related to C_e through the Gibbs–Thomson equation

$$C_i = C_e \exp\left(\frac{2\gamma V m}{r \mathrm{R} T}\right) \quad [12]$$

where γ is the particle-matrix interface energy, and V_m is the molar volume of the particle. Combining $\overline{C} = C_i$ and Eq. [12] leads to

$$r^* = \frac{2\gamma V m}{\mathrm{R}T} \left[\mathrm{In}\left(\frac{\overline{C}}{C_e}\right)\right]^{-1} \quad [13]$$

Finally for each radius, the evolution of the particle density N_v is given by

$$\frac{\partial N_v(r,t)}{\partial t} = -\frac{\partial}{\partial r}\left[N_v(r,t)\frac{dr}{dt}\right] + j \quad [14]$$

From the evolution of the distribution of particles size and density, the strengthening effects are deduced.[13] The solid solution hardening stress is the addition of the contributions of each element in solid solution:

$$\sigma_s = \sum_j k_j C_j^{2/3} \quad [15]$$

where C_j is the concentration of the specific alloying element in solid solution and k_j is the corresponding scaling factor.

The precipitate hardening stress is calculated from the particle density N_v, the mean radius $\bar{r}$, and the mean strength of the particles $\overline{F}$:

$$\sigma_p = \frac{M}{\mathbf{b}^2 \sqrt{G}} \sqrt{\frac{N_v \bar{r}}{\beta}} \overline{F}^{3/2} \quad [16]$$

where the particle strength F is related to the particle size through

$$F(r) = \begin{cases} 2\beta G\mathbf{b}^2\left(\frac{r}{r_c}\right) & \text{when } r \le r_c \\ 2\beta G\mathbf{b}^2 & \text{when } r > r_c \end{cases} \quad [17]$$

where r_c is the critical radius, and β is a numerical constant.

It should be noted that σ_s and σ_p calculated by Eqs. [15] and [16], respectively, are to be interpreted as *room temperature values* in the sense that the precipitate model (and its parameters) are fitted to room-temperature experiments only. In the present overall model, these room-temperature values are then "rescaled" to higher temperatures by the same factor $\chi(T)$ in Eq. [3] that also compensates for the too high dislocation density. The only input to the precipitate model is the alloy composition and the temperature history. In the present study, σ_s and σ_p are calculated by means of the Weldsim software[15] using prescribed temperature histories as input (Sections III–B and V).

D. *Implementation in FE Models*

In most FE models, the primary variable is the velocity (or displacement) from which the total strain rate tensor $(\dot{\varepsilon})$ is defined. This quantity is subdivided into an elastic part $(\dot{\varepsilon}^e)$, a thermal part $(\dot{\varepsilon}^T)$, and a viscoplastic part $(\dot{\varepsilon}^P)$:

$$\dot{\varepsilon} = \dot{\varepsilon}^e + \dot{\varepsilon}^T + \dot{\varepsilon}^P \quad [18]$$

where the effective viscoplastic strain rate in Eqs. 3 and 4, $(\dot{\bar{\varepsilon}}^p)$, equals $\sqrt{3/2\dot{\varepsilon}^P : \dot{\varepsilon}^P}$ under the assumption that there are no volume changes associated with the viscoplastic deformation. The elastic and thermal parts are related to the stress tensor and temperature by Hooke's law and the law of thermal expansion, respectively.

Along with the usual relations between tensors and effective scalar measures for stress and viscoplastic strains in isotropic materials, the set of equations in the present section enables the calculation of the viscoplastic strain rate considering the total strain rate and temperature as known input. This general formulation allows the integration of the constitutive equations for any input evolution in temperatures and total strain rate tensor, which is the usual situation in most FE codes as well as in experimental tensile tests.

III. PARAMETER DETERMINATION

The parameters of governing Eqs. [2] through [8] have to be tuned to the relevant alloy. The same applies to the "precipitate strength" parameters β and r_c in Eq. [17], while the calculation of the nucleation, growth, and dissolution of the precipitates relies in the present study entirely on the model (and model parameters) presented in Reference 11; the modeling Eqs. [9] through [17] being solved by Weldsim.[15] In the present study, the parameters are determined by fitting calculated tensile stress-strain curves at constant temperatures and varying strain rates to similar experimental curves for an AA6060 aluminum alloy, reported in Reference 15.

A. *The Gleeble Tests of Reference 15*

The Gleeble tests in Reference 15 were carried out on specimens taken from an AA6060 aluminum alloy with Mg 0.43 wt pct and Si 0.44 wt pct as the main alloying elements. The tensile testing was carried out at temperatures and strain rates in the range 20 °C to 340 °C and 10^{-4} to 10^{-2} s^{-1}, respectively. Extruded profiles with a thickness of 1.8 mm were cut into bone-shaped test specimens with a straight 30-mm- and 8-mm-wide central section. The samples were solution heat treated, water quenched, and artificially aged for 9 hours at 170 °C to reach the peak-aged (T6) condition. The elongation of a 10-mm section was measured by an extensometer. The samples were first strained to 6 pct at a constant temperature. A rapid heating cycle was then imposed with a peak temperature of 540 °C, and a rapid cooling to the previous deformation temperature followed by additional 8 to 10 pct straining at the same constant temperature as the previous straining. In both straining periods, the strain rate was increased by a factor of 10 from a value of about 10^{-3} s^{-1}, after a first 2 to 4 pct straining.

Figure 3 shows measured evolutions of temperature in the specimen center, stress, and accumulated strain in experiment D at temperature of 340 °C in Reference 15. The temperature peak at 540 °C implies complete precipitate dissolution, and thus a completely changed material state. The analysis of these tensile tests has therefore been subdivided into two parts: before and after the temperature peak. In both parts, the initial value of the dislocation density has been set equal to a low value, 10^{12} m^{-2}. This value is assumed to reflect the dislocation density after the T6 heat treatment prior to any deformation of the specimen as well as the dislocation density after heating to 540 °C prior to the second part of the tensile test; the latter heating process leading to static recovery of the dislocations accumulated during the first straining. Table II summarizes the experiments and their denomination in subsequent sections.

In correspondence with the experimental situation, the total strain rate (not the viscoplastic part of the strain rate), and a constant temperature are used as input when the Gleeble tests have been simulated. Also, a thermal part is added to the strain rate in order to account for the thermal expansion (during heating) and contraction (during cooling) of the Gleeble specimen. Please note that the total strain rate histories have been smoothed to suppress the experimental oscillations.

B. *Parameter Fit to the Gleeble Tests*

The parameters and their variation with temperature have been determined by a stepwise procedure, and the tuning is based on a simple visual comparison between the experimental and modeled curves. Treating

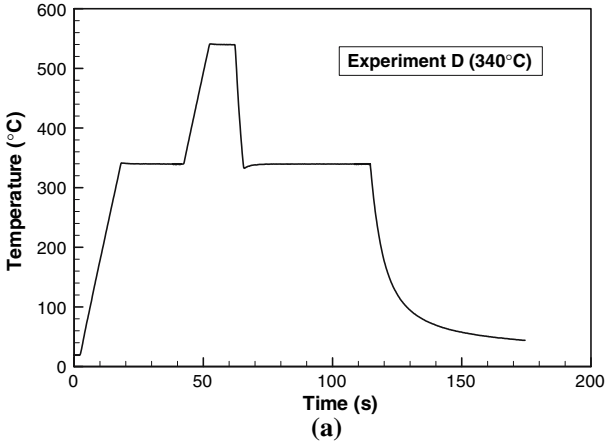

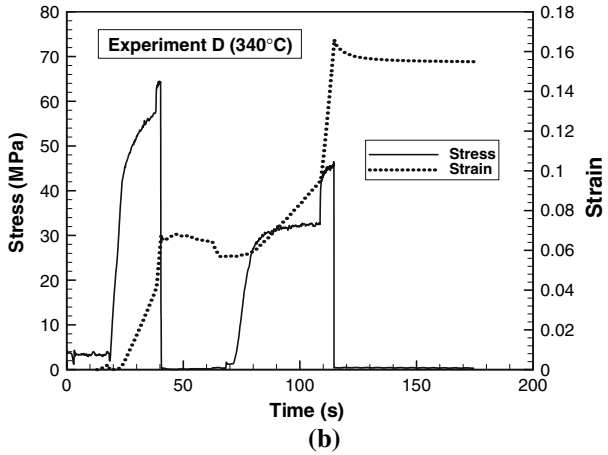

Fig. 3—Histories of (*a*) temperature and (*b*) stress and strain from the Gleeble experiments.

separately and successively the parameters obtained quite good fit.

The Zener–Hollomon parameters *a, n, Q*, and *A* in Eqs. [7] and [8], were determined first. These relations are assumed to apply at high temperatures and for a material in the solid solution state. Experiment D-SSS, for which the resulting curve is displayed in Figure 4, fulfills these conditions. The parameters of the Zener–Hollomon relation were first set equal to values fitted previously for an AA6060 alloy.[‡] Then a comparison with experiment D-SSS was made to tune more precisely their values. It turned out that keeping *a*, *n*, and *A* as previously along with a slight change in the value of *Q* (from 156 to 161 KJ/mol in the present study) leads to a quite accurate match to the two saturation stresses observed before and after the strain rate jump in Figure 4. Please note that there is no physical basis for this change in *Q*; it was simply made for obtaining a better fit to the experimental data. The final values of the Zener–Hollomon parameters are given in Table I.

As the experiments listed in Table II are limited to 340 °C, a comparison with an additional experiment has been made to validate the values of the Zener–Hollomon parameters. In this case, the specimen was heated to 500 °C and then put in tension at different constant values of the stress; the evolution of the stress and the strain are plotted in Figure 5. The corresponding strain rates of the three higher plateaus are also indicated. The stress levels predicted by Eq. [7] for these strain rates are compared to the experimental stress levels in Table III. These modeling results are in acceptable agreement with the experimental results.

[‡]Unpublished research.

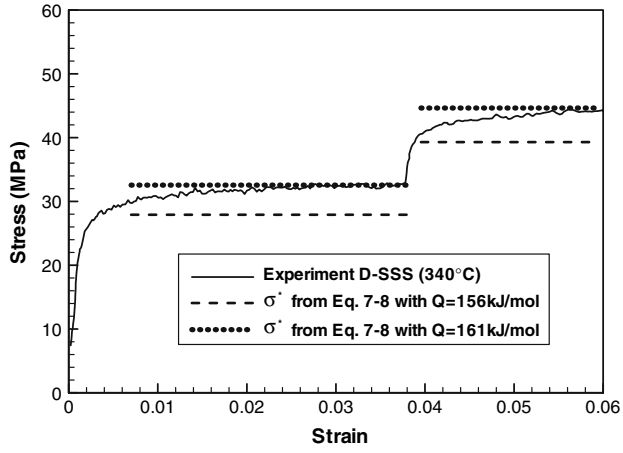

Fig. 4—Fitting of the saturation stress predicted with the Zener–Hollomon relation to experiment D-SSS.

In Reference 11, the precipitation model was tuned for another alloy, AA6005, and the material strength was determined by hardness measurements. Due to the difference in composition between the two alloys as well as the inaccuracy in relating hardness to yield stress, the hardening contributions from elements in solid solution and precipitates have been rescaled in order to obtain a better fit to the present experiments using an AA6060 alloy

$$\sigma_s + \sigma_p = \frac{0.33\left(\sigma_s^W + \sigma_p^W\right) - 3}{0.26} \qquad [19]$$

where *W* indicates the output from Weldsim. A further adjustment of the precipitate strengthparameters β and r_c was then carried out. Three different tensile test results were used for this purpose: A-ini, B-ini and C-ini. In the first two cases, $\sigma_s + \sigma_p$ was calculated from the measured yield stress. At this transition point between elastic and plastic behavior, we assume that the dislocation density is still at its initial level ρ_0 and the viscoplastic strain rate is nearly equal to the total strain rate. Then $\sigma_s + \sigma_p$ is equal to $\sigma\left(\frac{\dot{\varepsilon}}{\dot{\varepsilon}_0}\right)^{-1/m} - \sigma_\perp^0$ where $\sigma_\perp^0$ is related to ρ_0 by Eq. [2]. In experiment C-ini, two saturation stresses were reached for two different strain rates. After an initial estimate of the strain rate sensitivity *m* along similar lines as those discussed in connection with Figure 2, the difference between the saturation stress with the current precipitate state and the saturation stress for a precipitate-free material given by Eqs. [5] through [8] was determined. The value of the precipitate stress was then determined by setting χ equal to 1 and

Table I. Nomenclature

Symbols	Variables	Unit
σ	stress	MPa
$\sigma_\perp$	dislocation stress	MPa
σ_s	solute contribution to the precipitate stress	MPa
σ_p	precipitate contribution to the precipitate stress	MPa
$\hat{\sigma}$	hardening stress	MPa
σ^*	saturation stress	MPa
$\dot{\varepsilon}$	total strain rate	s^{-1}
$\dot{\varepsilon}^p$	viscoplastic strain rate	s^{-1}
$\dot{\varepsilon}^e$	elastic strain rate	s^{-1}
$\dot{\varepsilon}^T$	thermal strain rate	s^{-1}
ρ	dislocation density	m^{-2}
ρ^*	saturation dislocation density	m^{-2}
N_v	precipitate density	$\#/m^3$
$\overline{F}$	mean obstacle strength	MPa/m
T	temperature	K
$\overline{C}$	mean solute concentration	wt pct
C_e	equilibrium solute concentration	wt pct
C_p	particle solute concentration	wt pct
C_i	interface solute concentration	wt pct
α_T	thermal dilatation coefficient	K^{-1}
r	particle radius	M
ZH	Zener–Hollomon variable	—

	Parameters	Value
M	average Taylor factor	3.06
E	Young's modulus	70,000 MPa (room temperature)
G	shear modulus	27,000 MPa (room temperature)
b	burger's vector	$2.84 \cdot 10^{-10}$ m
α	numerical constant	0.3
$\dot{\varepsilon}_0$	reference strain rate	60,000 s^{-1}
m	strain rate sensitivity	temperature dependency relation (Table IV)
χ	hardening factor	temperature dependency relation (Table IV)
ρ_0	initial dislocation density	10^{12} m^{-2}
k_1	dislocation storage coefficient	$2.7 \cdot 10^8$ m^{-1}
k_2	dynamic recovery coefficient	from Zener–Hollomon relation (Eq. [5])
D	solute diffusivity	$2.2 \cdot 10^{-4}$ m^2/s
j_0	reference nucleation rate	$3.07 \cdot 10^{36}$ $\#/m^3/s$
A_0	energy barrier for nucleation	18 kJ/mol
Q_d	diffusion activation energy	130 kJ/mol
β	numerical constant	0.53
r_c	critical radius	$5.7 \cdot 10^{-9}$ m
γ	particle-matrix interface energy	0.26 J/m^2
V_m	molar volume of the particle	$7.62 \cdot 10^{-5}$ m^3/mol
T_c	critical temperature	423 K
a	reference stress in ZH relation	30 MPa
Q	activation energy in ZH relation	161 kJ/mol
A	reference strain rate in ZH relation	$2.35 \cdot 10^{10}$ s^{-1}
n	exponent in ZH relation	4.1

represents number of particle per unit volume.

the values of the precipitate strength parameters are given in Table I.

The determination of k_1 is almost entirely based upon experiment A-ini. The reason for this choice is twofold; first, there is no strain rate sensitivity at room temperature; and second, σ_p does not change during room-temperature testing after a T6-heat treatment. Furthermore, we have observed that this constant room-temperature value of k_1 (Table I) gives a satisfactory fit to the experimental curves also at the higher temperatures, which is demonstrated in the final simulations of the tensile tests displayed in Figure 8. A similar conclusion was given by Estrin,[6] where the coefficient k_1 is related to the mean free path of the dislocations. Please note that once k_1 has been determined, k_2 (being temperature dependent) is given by Eqs. [5] through [8].

Experimental results from A-ini, B-ini, C-ini, and D-SSS were used for determining the parameters m and χ. First, at each temperature separate fittings provided

Table II. Summary of the Gleeble Experiments[15]

Name	Temperature	Initial Material State
A-ini	20 °C	T6 heat treatment
A-SSS	20 °C	solute solution
B-ini	150 °C	T6 heat treatment
B-SSS	150 °C	solute solution
C-ini	250 °C	T6 heat treatment
C-SSS	250 °C	solute solution
D-ini	340 °C	T6 heat treatment
D-SSS	340 °C	solute solution

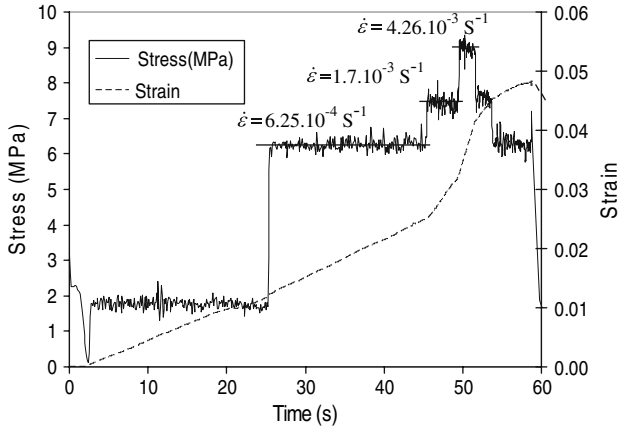

Fig. 5—Evolution of the stress and strain for the specimen deformed at 500 °C. The mean values of the stress at the three higher plateaus are indicated by lines.

Table III. Comparison of Zener–Hollomon Predictions with the Experiment Conducted at 500 °C

Strain Rate	Measured Stress	Predicted Stress
$6.25{\cdot}10^{-4}\ s^{-1}$	6.3 MPa	6.5 MPa
$1.7{\cdot}10^{-3}\ s^{-1}$	7.5 MPa	8.3 MPa
$4.26{\cdot}10^{-3}\ s^{-1}$	9.0 MPa	10.3 MPa

values for m and χ, and the temperature dependency relation for m was determined. Applying this relation, a second set of values for χ was obtained by a new fitting to the selected experiments, and a temperature dependency relation for χ was deduced. These two steps were iterated until a satisfactory fit to the selected experiments was achieved using simple relations for m and χ temperature dependencies. Moreover, the evolution of the saturation dislocation density at higher temperatures must be realistic. Therefore, the extrapolation of the evolution of χ at higher temperatures was made by assuming a smooth evolution of the dislocation density at saturation as shown in Figure 6. With this additional assumption, the final relations were obtained. They are given in Table IV and plotted in Figure 7. Please note that the extrapolation of these relations to very small strain rates at high temperatures leads to small negative dislocation densities. A minimum dislocation density has therefore been defined, with the consequence that the saturation stress is overestimated in this critical case.

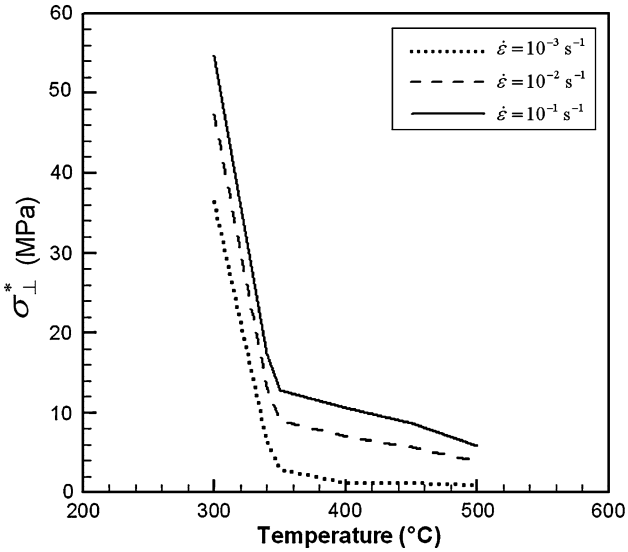

Fig. 6—Evolution of the dislocation stress at saturation at different strain rates as a function of temperature.

Table IV. Temperature Dependency Relations for m and χ

$m = 320\ \exp\ [-0.0121 \cdot (T - 298)] + 4$	
$\chi = 4.6 \cdot \left[\tanh\left(\frac{T-614}{51}\right) + 1\right] + 1$	if $T \le 623$ K
$\chi = 0.0313\ T$–13.1	if $T > 623$ K

As far as the strain rate sensitivity m is concerned, this parameter has already been initially estimated by examining the stress jump caused by a jump in total strain rate. It turns out that the second fitting presented in the previous paragraph only changes the m values at the different temperatures slightly compared to those values obtained by the initial estimate.

As the parameter determination is completed, the simulation results are compared with the experimental stress-strain curves in Figure 8. It is seen that the parameter values and temperature dependency relations obtained by the fitting procedure leads to a satisfactory fit to the experimental results.

IV. DISCUSSION

A. *A Simplified Modeling Approach*

Age-hardened aluminum alloys have a microstructure that changes during heat treatment. In solid solution, the alloying elements are completely dissolved and the material behaves like a single-phase material in which the major microstructure feature is the grain boundaries. During aging, the alloying elements cluster and start forming small hardening precipitates, which are initially weak and coherent and thus shearable by dislocations. Further aging leads to coarsening of the microstructure. Larger incoherent particles are formed near the peak hardness that are not shearable by dislocations. A change in the dislocation strengthening mechanism from particle shearing to bypassing *via* Orowan looping

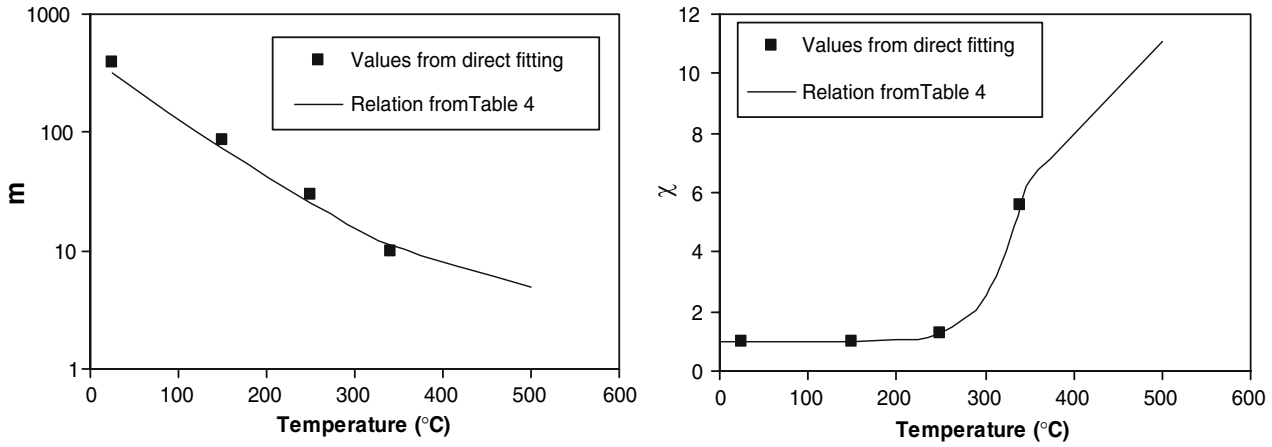

Fig. 7—Approximation of the temperature dependency of m and χ.

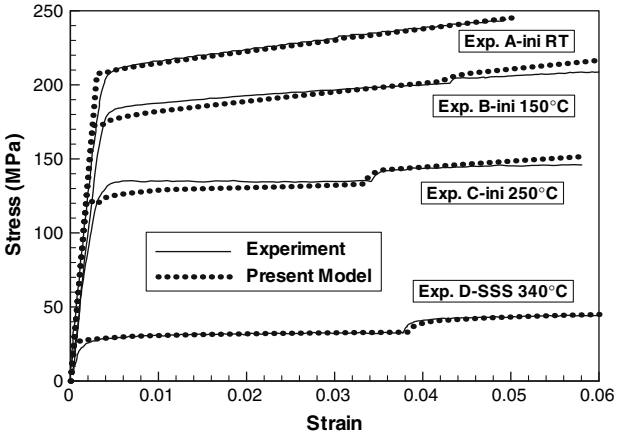

Fig. 8—Comparison of the stress-strain curves for experiments A-ini, B-ini, C-ini, and D-SSS.

takes place as the coarsening process proceeds. In addition, precipitate-free zones will form adjacent to the grain boundaries because of nucleation and growth of coarse precipitates at the grain boundaries. The microstructure thus becomes inhomogeneous and quite complex when the material is age hardened.

When an age-hardened aluminum alloy is subjected to plastic deformation at elevated temperatures, coarsening or dissolution of the hardening precipitates will occur. At the same time, the dislocation density increases rapidly through multiplication (*e.g.*, by activation of Frank–Read sources), which contributes to the work hardening due to dislocation-dislocation and particle-dislocation interactions. The material will respond to this deformation by forming a cell structure in which the dislocations accumulate partly in the cell walls and partly within the cell interiors. A full subgrain microstructure develops at large deformations, consisting of low-angle grains with a well-defined misorientation. In addition, localization of deformation to the precipitate-free zones occurs that in turn leads to extensive strain accumulation in the soft regions adjacent to the grain boundaries.

It would obviously be a considerable task to model the evolution of the deformation microstructure during

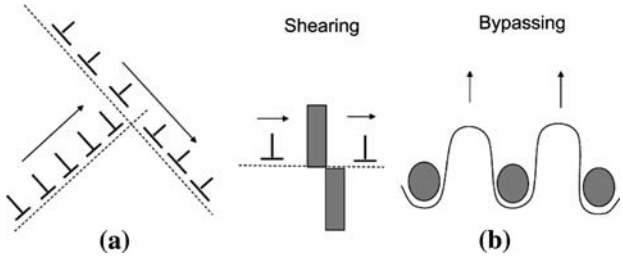

Fig. 9—Schematic representation of the proposed work-hardening model for age-hardened aluminum alloys: (*a*) dislocation-dislocation interactions and (*b*) particle-dislocation interactions.

plastic deformation at elevated temperatures in its entirety and then, on the basis of dislocation mechanics, develop constitutive equations for the resulting stress-strain behavior. The model presented in this study is therefore based on a quite pragmatic and idealized work-hardening model for age-hardened aluminum alloys by which the flow stress can be calculated as a function of temperature and viscoplastic strain rate that changes with time during the thermomechanical operation. As indicated in Figure 9, the two main mechanisms being accounted for in the work-hardening model are the dislocation-dislocation interactions and the particle-dislocation interactions; the latter contribution includes both shearing and bypassing of the particles by the dislocations. These two hardening contributions are modeled by means of internal variables representing the total dislocation density, ρ, and the intrinsic resistance F of the hardening precipitates to dislocation motion, respectively. Updated values for ρ and F are then obtained by solving a set of nonlinear ordinary differential equations for the evolution of the relevant microstructural parameters with time, considering the time evolutions of temperature and strain rate as input.

B. *Some Specific Limitations in the Present Model*

Four of the Gleeble tests presented in Reference 15 (D-ini, A-SSS, B-SSS, and C-SSS in Table II) were not applied for the parameter fit, and comparing results

predicted by the present model and these four tests reveals some limitations in the model. These are associated with the following phenomena to be discussed in the subsequent paragraphs: overestimation of the precipitate stress and precipitate-dislocation interaction.

The D-ini experimental curve is shown in Figure 10 along with the results from a modeling of this test. The modeling of experiment D-ini resulted in too high stress values. It is, however, reasonable to believe that the particular experimental situation for experiment D-ini is critical for the precipitate model due to the specific thermomechanical history. This history implies that the large precipitates grow at the expense of the small precipitates during heating that significantly changes the material from an initial T6 temper to a soft material, followed by deformation during which the dislocation hardening develops significantly. These are conditions for which the applied precipitate model has not been tuned.[10,11] Nevertheless, an acceptable fit to the experimental stress-strain curve *can* be obtained simply by subtracting 23 MPa from the value of σ_p, in order to account for the loss of precipitation hardening induced by the heating (Figure 10).

Another limitation of the precipitate model is that the incubation time for precipitate nucleation[10,11] is neglected. Therefore, it is reasonable to believe that the precipitate stress is overestimated during the cooling stage after the temperature peak, as indicated in Figure 11(a). For example, a relatively high degree of nucleation during cooling in experiment A-SSS is predicted by the model, while none is expected to occur for the specific AA6060 alloy.[20] As shown in Figure 11(b), the predicted yield stress is thus higher than the measured value. Similar results are obtained when experiment B-SSS is simulated, while no significant strengthening is expected during this test (around 1 minute at 150 °C), even with some strain-induced precipitation. Finally, for experiment C-SSS, the assumption of zero incubation time leads to an overestimation of the precipitate hardening during all the deformation.

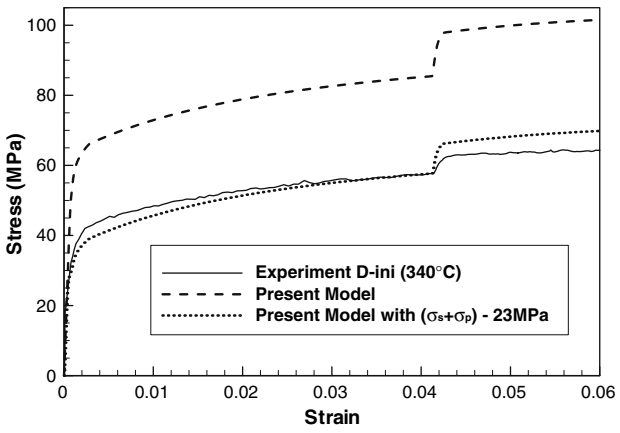

Fig. 10—Comparison of the measured stress-strain curve with a simulation using the fitted parameters tabulated in Section III–B, and a *new* simulation using the same parameters but with a lower precipitate hardening $(\sigma_s + \sigma_p)^{new} = \sigma_s + \sigma_p - 23$.

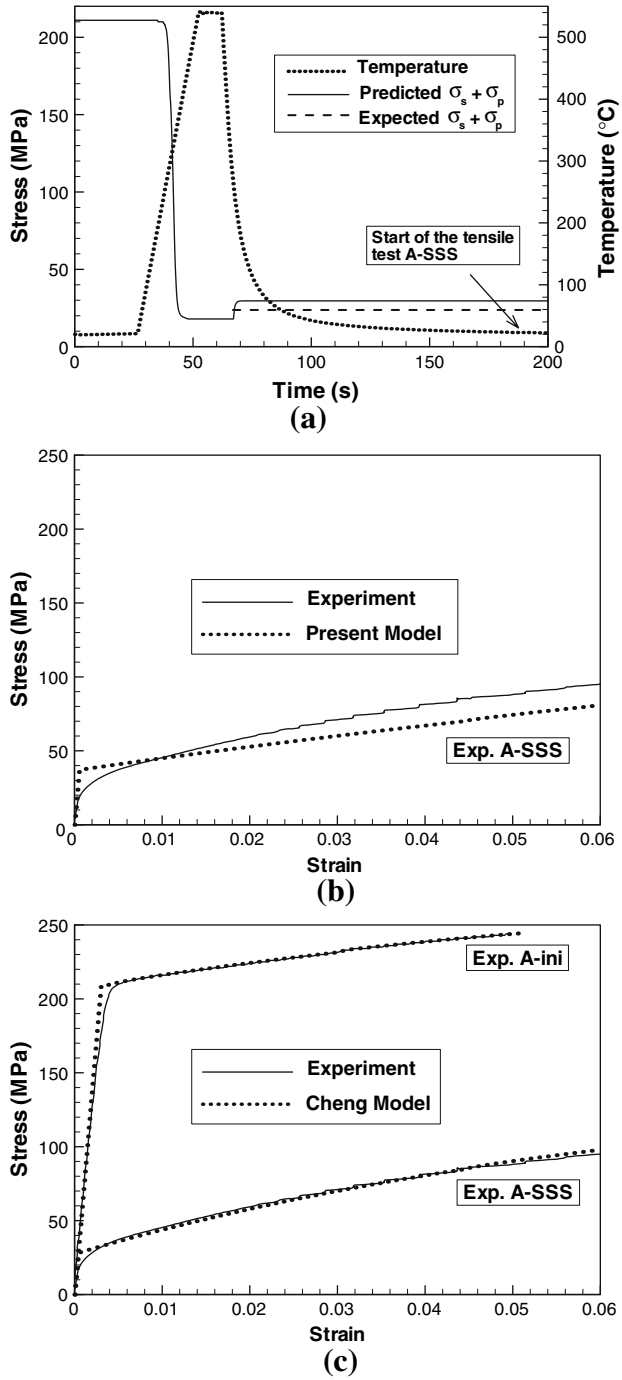

Fig. 11—Modeling and test results for experiment A-SSS. (*a*) Temperature and modeled precipitate stress evolution along with expected $\sigma_s + \sigma_p$ evolution. (*b*) Stress-strain curves using present model (Eq. [2]). (*c*) Stress-strain curves using Cheng *et al.*[8] model (Eq. [20]).

The modeled curve for experiment A-SSS shown in Figure 11(b) also reveals a discrepancy in the work-hardening rate, which is not related to the precipitate model simply because there is no significant change in the precipitate state at room temperature. In other words, the parameter value for k_1 (which controls the stress curve slope, Eq. [4]) determined on the basis of experiment A-ini only, does not give a very accurate fit

when experiment A-SSS is modeled. This difference in slope can be explained by the fact that the interactions between the dislocations and the precipitates depend on the precipitate size. Cheng *et al.*[8] have adopted the superposition law suggested by Kocks in which the solid solution hardening is included and the precipitate and dislocation hardening contributions are added according to the relation

$$\hat{\sigma} = \sigma_s + \left(\sigma_{\perp}^{\nu} + \sigma_p^{\nu}\right)^{1/\nu} \quad [20]$$

where, σ_s, σ_p, and $\sigma_{\perp}$ denote the solid solution, the precipitate, and the dislocation hardening contributions, respectively, exactly as seen previously in the present article. The exponent ν can vary between 1 and 2; $\nu = 1$ applies in the case of high density of weak barriers and low density of strong barriers as in underaged temper. When the barriers are identical, $\nu = 2$ as in the overaged temper. Replacing Eq. [2] with Eq. [20], a simultaneous fit of k_1 and ν using both experiments A-ini and A-SSS has thus been carried out, assuming a constant "precipitate-free" state ($\sigma_p = 0$) for experiment A-SSS. The resulting parameter values are $\nu = 1.15$ and 1 for A-ini and A-SSS, respectively, and $k_1 = 5.8 \cdot 10^8$ m^{-1}; the stress-strain curves are shown in Figure 11(c). It is seen that the elaborated approach quite accurately fits the experiments. While the hardening Eq. [2] suggested by Estrin[6] has been applied in the present work for the sake of simplicity, the results based on using Eq. [20] indicate the need for a more elaborate model. The approach in Reference 8 does, however, require additional information about the precipitates (shearable/nonshearable), and in addition, Cheng *et al.*[8] indicate that the dislocation density evolution equation (Eq. [4]) must also take into account the two kinds of particles.

V. APPLICATION

This last section is devoted to elucidating the applicability of the constitutive model in FE simulations of hot forming. The modeling equations are solved using an evolution of temperature and total strain rate that reflects some aspects of hot forming as input. The resulting evolution in flow stress during the viscoplastic deformation has then been discussed in the light of the corresponding evolutions in dislocation hardening stress, $\sigma_{\perp}$ and the sum of solid solution and precipitate hardening stresses, $\sigma_s + \sigma_p$. Also, the effects on the flow stress of temperature level and strain rate at different temperatures have been discussed, and the study demonstrates the ability of the model to handle quite complex evolutions in temperature and strain rate.

The applied temperature and total strain rate evolutions input are shown in Figure 12(a). A temperature cycle from room temperature to room temperature is imposed with a quite fast initial heating, which reflects some main aspects of hot forming operation. The cycle includes a period at 400 °C, during which the smallest precipitates dissolve and the largest grow, followed by a period at 250 °C, during which all particles grow further. Finally, there is a period of cooling down to room temperature during which the amount of precipitates remains constant. All these aspects are reflected in the calculated evolution of $\sigma_s + \sigma_p$ in Figure 12(b), which results by solving Eqs. [9] through [17] using the temperature evolution in Figure 12(a) as input. Furthermore, it is seen in Figure 12(a) that different strain and strain rate jumps are imposed during various parts of the temperature history. The calculated evolution in effective viscoplastic strain rate is also shown in Figure 12(a), which as expected is very close to that for the total effective strain rate when the material is outside the typical elastic response regimes. In addition to the evolution of $\sigma_s + \sigma_p$ the evolutions of the flow stress σ and dislocation stress $\sigma_{\perp}$ are also displayed in Figure 12(b); the latter quantity being proportional to the square root of the dislocation density by Eq. [2].

Although reflecting some main aspects of hot forming, the input has been chosen such that the modeling results should not be affected too much by the limitations in the present version of the model discussed in the previous section. More specifically, the input represents a situation in which there is not any strong precipitate dissolution during deformation, there is no cooling to room temperature after a temperature peak, there is no deformation at low temperatures in the precipitate-free state, the initial dislocation density is not too high, and the strain rate at high temperatures is not too low. Furthermore, the total strain rate was chosen such that the material remains in tensile condition even with thermal expansion.

It is seen in Figure 12(b) that there is an increase in the dislocation stress (and thus the dislocation density) during the first deformation followed by an approximately constant value when the strain rate drops. There is then a drop in dislocation stress due to dynamic recovery associated with the straining during the temperature increase between 5 and 7 seconds. Due to the low strain rate sensitivity at 200 °C, the jumps in strain rate during this period of constant temperature and precipitate stress only lead to changes in the work-hardening rate. On the other hand, the strain rate jump is much more significant at 400 °C, at which the stress is close to the saturation value given by Eqs. [5] through [8]. Around 10 seconds, there is again a decrease in dislocation stress caused by dynamic recovery. During the heating from 200 °C to 400 °C, there are two sudden decreases in flow stress, first due to the decrease in strain rate after 4.5 seconds, and then due to the decrease in precipitation stress from 6 seconds. When the constant temperature of 250 °C has been reached (around 15 seconds), the flow stress increases due to the increase in precipitation stress, even though the effective viscoplastic strain rate, and thus the increase in dislocation stress, is very small. There are significant jumps in flow stress at 19 and 29 seconds due to the strain rate increase and decrease at these two points in time, and between 19 and 29 seconds there is a significant flow stress increases because of the combined effects of dislocation and precipitation hardening. The final increase in flow stress is due to the decreasing temperature from 30 seconds.

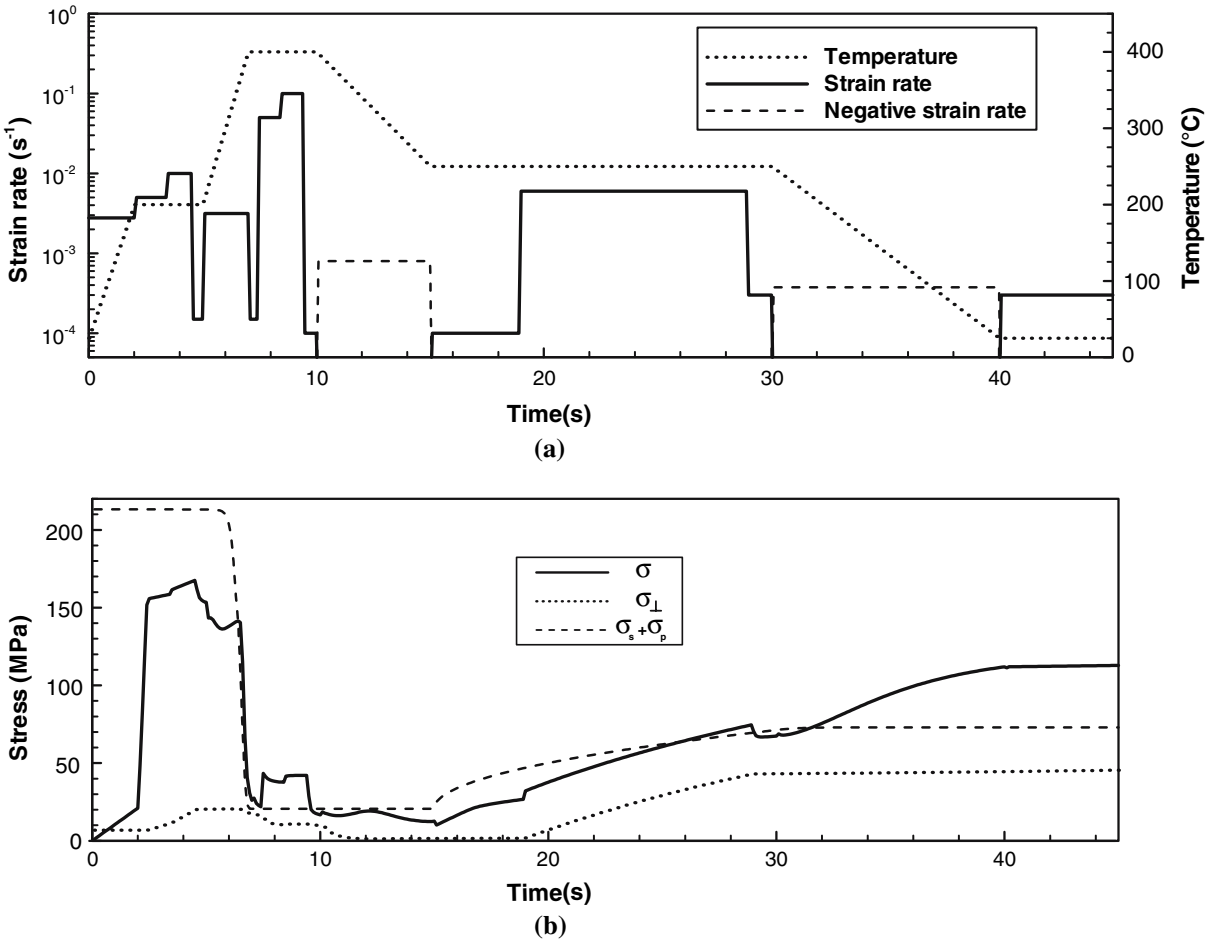

Fig. 12—(*a*) Temperature and total strain rate evolutions (boldfaced) used as input to the case study along with the calculated evolution in effective viscoplastic strain rate (nonboldfaced); the strain rates with logarithmic axis at the right, and with negative values indicated by dots. (*b*) Calculated evolutions of the flow stress, dislocation stress, and precipitate stress.

The dislocation stress is nearly constant in this last period due to the low strain rate; also the precipitation stress is constant.

Finally, it is mentioned that the present constitutive model was recently applied in a case study[21] directed toward local hot forming. Modeling results were compared to those obtained when the internal variable model was interchanged by the simpler "classical" approach based on a set of hardening curves to fit tensile data. The case study clearly revealed that the evolution of the dislocation density and the precipitates can have a significant effect upon the flow stress during local hot forming operations.

VI. CONCLUSIONS

A new internal variable constitutive model for the use in FE simulation of local hot forming of 6xxx aluminum alloys has been presented. The model relates the flow stress to the temperature, total strain rate, and internal variables, which represent the dislocation density and the contributions to the hardening stress from elements in solid solution and precipitates. The model is able to reproduce some main features appearing in local hot forming. Complementary experiments are, however, required for assessing the accuracy of the constitutive model for complex temperature and strain rate histories. It is believed that further development of the model should include a more accurate description of the interactions between the dislocations and the precipitates, *e.g.*, by differentiating shearable and nonshearable particles, and modifying the calculation of the dislocation accumulation and the summation of the different contributions to the hardening stress accordingly. Also the effect of static recovery should be quantified and incorporated in the constitutive model.

ACKNOWLEDGMENT

Financial support from the Research Council of Norway through Project No. 158918/130 *Computer Aided Local Thermal Manipulation of Aluminium Alloys* managed by the Institute for Energy Technology, Norway, is greatly acknowledged.

REFERENCES

1. H. Takuda, K. Mori, I. Masuda, Y. Abe, and M. Mastuo: *J. Mater. Process. Technol.*, 2002, vol. 120, pp. 412–18.
2. M. Keigler, H. Bauer, D. Harrison, and A.K.M. De Silva: *J. Mater. Process. Technol.*, 2005, vol. 167, pp. 363–70.
3. B.W. Tveiten, A. Fjeldstad, G. Härkegård, O.R. Myhr, and B. Bjørneklett: *Int. J. Fatigue*, 2006, vol. 28, pp. 1667–76.
4. B. Bjørneklett, O.E. Myhr, and P. Vist: Patent Application WO 2005/077560 A1, Aug. 2005.
5. U.F. Kocks: *J. Eng. Mater. Technol*, 1976, vol. 98, pp. 76–85.
6. Y. Estrin: in *Unified Constitutive Laws of Plastic Deformation*, A.S. Krausz and K. Krausz, eds., Academic Press, San Diego, 1996, pp. 69–106.
7. X. Wang, W.J. Poole, S. Esmaeili, D.J. Lloyd, and J.D. Embury: *Metall. Mater. Trans. A*, 2003, vol. 34A, pp. 2913–24.
8. L.M. Cheng, W.J. Poole, J.D. Embury, and D.J. Lloyd: *Metall. Mater. Trans. A*, 2003, vol. 34A, pp. 2473–81.
9. A. Deschamps, D. Solas, and Y. Bréchet: in *Microstructure Properties and Processes*, Proc. Euromat 99, München, Germany, Y. Bréchet, ed., Wiley-VCH, New York, 1999, vol. 3, pp. 121–132.
10. O.R. Myhr, Ø. Grong, and S.J. Andersen: *Acta Mater.*, 2001, vol. 49, pp. 65–75.
11. O.R. Myhr, Ø. Grong, H.G. Fjær, and C.D. Marioara: *Acta Mater.*, 2004, vol. 52, pp. 4997–5008.
12. A. Deschamps and Y. Bréchet: *Acta Mater.*, 1999, vol. 47, pp. 293–305.
13. S. Esmaeili, D.J. Lloyd, and W.J. Poole: *Acta Mater.*, 2003, vol. 51, pp. 2243–57.
14. A.H. Van den Boogaard and J. Huétink: *Comput. Methods Appl. Mech. Eng.*, 2006, vol. 195, pp. 6691–6709.
15. H.G. Fjær, B.I. Bjørneklett, and O.R. Myhr: *Proc. TMS Annual Meeting*, San Francisco, CA, Feb. 2005, TMS, Warrendale, PA, 2005, pp. 95–100.
16. C. Zener and J.H. Hollomon: *J. Appl. Phys.*, 1944, vol. 15 (1), pp. 22–32.
17. F. Roters, D. Raabe, and G. Gottstein: *Acta Mater.*, 2000, vol. 48, pp. 4181–89.
18. F. Garofalo: *Fundamentals of Creep and Creep-Rupture in Metals*, MacMillan Company, New York, NY, 1965, pp. 51–55.
19. A.K. Miller: in *Unified Constitutive Equations for Creep and Plasticity*, A.K. Miller, ed., Elsevier Applied Science, London, 1987, pp. 139–219.
20. A.K. Gupta, D.J. Lloyd, and S.A. Court: *Mater. Sci. Eng.*, 2001, vol. A316, pp. 11–17.
21. S. Gouttebroze, A. Mo, and H.G. Fjær: *Proc. TMS Annual Meeting*, Orlando, FL, Feb. 2007, pp. 109–18.